

See discussions, stats, and author profiles for this publication at: <https://www.researchgate.net/publication/229432426>

Superior Catalytic Effects of Nb₂O₅, TiO₂, and Cr₂O₃ Nanoparticles in Improving the Hydrogen Sorption Properties of NaAlH₄

ARTICLE in THE JOURNAL OF PHYSICAL CHEMISTRY C · MAY 2012

Impact Factor: 4.77 · DOI: 10.1021/jp302474c

CITATIONS

18

READS

25

9 AUTHORS, INCLUDING:



Rafiud Din

Pakistani Institute of Engineering and Applie...

58 PUBLICATIONS 383 CITATIONS

[SEE PROFILE](#)



Xuanhui Qu

University of Science and Technology Beijing

524 PUBLICATIONS 3,131 CITATIONS

[SEE PROFILE](#)



M. Zubair Iqbal

Chinese Academy of Sciences

45 PUBLICATIONS 201 CITATIONS

[SEE PROFILE](#)



Islamud Din

International Islamic University, Islamabad

13 PUBLICATIONS 57 CITATIONS

[SEE PROFILE](#)

Superior Catalytic Effects of Nb_2O_5 , TiO_2 , and Cr_2O_3 Nanoparticles in Improving the Hydrogen Sorption Properties of NaAlH_4

Rafi-ud-din,^{*,†,‡} Qu Xuanhui,^{*,†} Li Ping,[†] Lin Zhang,[†] Wan Qi,[†] M. Zubair Iqbal,[§] M. Yasir Rafique,[§] M. Hassan Farooq,[†] and Islam-ud-din^{||}

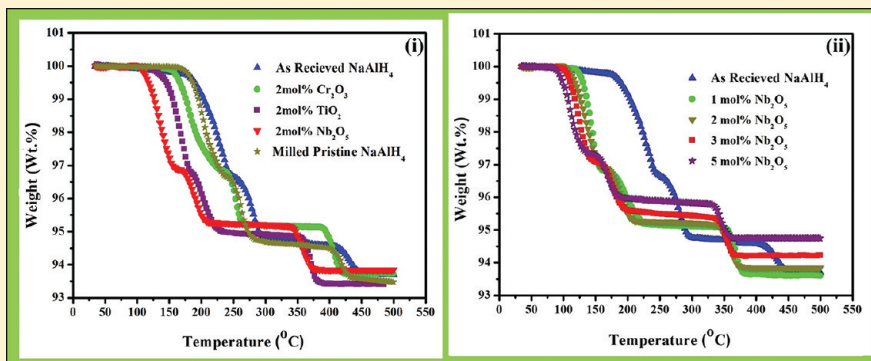
[†]State Key Laboratory for Advanced Metals and Materials, School of Materials Science and Engineering, USTB, Beijing 100083, China

[‡]Chemistry Division, PINSTECH, P.O. Office, Nilore, Islamabad, Pakistan

[§]Department of Physics, School of Applied Science, University of Science and Technology Beijing, Beijing 100083, P. R. China

^{||}Department of Environmental Sciences, International Islamic University, Islamabad, Pakistan

Supporting Information

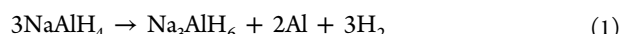


ABSTRACT: Sodium alanate (NaAlH_4) is a promising complex metal hydride due to its reasonable hydrogen storage capacity (7.4 wt %). However, the pristine NaAlH_4 suffers from the inherent limitations of unfavorable thermodynamics (high desorption temperature), slow kinetics, and poor reversibility. In the present work, the efficacy of Nb_2O_5 , TiO_2 , and Cr_2O_3 nanoparticles in ameliorating hydrogen sorption properties of NaAlH_4 was evaluated. The use of Nb_2O_5 and TiO_2 displayed superior catalytic effects in terms of enhancing dehydridding/rehydridding kinetics and reducing the dehydrogenation temperature of NaAlH_4 . Isothermal volumetric measurements at 150 °C revealed that kinetics of hydrogen desorption with Nb_2O_5 and TiO_2 were almost 11–12 times that of pristine NaAlH_4 . The apparent activation energy as well as enthalpy of dehydrogenation were considerably lowered by addition of Nb_2O_5 and TiO_2 nanopowders. Moreover, the pronounced enhancement on hydrogen capacity arising upon adding Nb_2O_5 and TiO_2 was observed to persist well in rehydrogenation/dehydrogenation cycles. X-ray diffraction (XRD), X-ray photoelectron spectroscopy (XPS), Fourier transform infrared (FTIR), and FESEM-EDS analyses demonstrated that reduction of Nb_2O_5 and TiO_2 during the first desorption was coupled to the migration of reduced titanium oxide species from surface to bulk during cycling. It was suggested that these finely dispersed oxygen-deficient niobium and titanium species might contribute to kinetic improvement by facilitating the hydrogen diffusion during both dehydrogenation/rehydrogenation.

INTRODUCTION

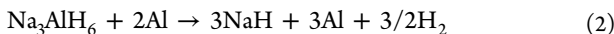
Onboard hydrogen storage has been recognized as one of the key scientific challenges in realizing the successful implementation of hydrogen economy. According to the U.S. DOE's 2015 targets, a viable hydrogen storage system has necessitated the hydrogen storage materials with more than 5.5 wt % capacity and fast desorption kinetics (1.5 wt %/min). The combined stringent requirements on energy density, discharging/recharging kinetics, and reversibility for the onboard H-storage system have largely frustrated numerous efforts on various metal hydrides.^{1–3} Alanate-based complex metal hydrides^{4–15} have high gravimetric and volumetric hydrogen storage densities but have not been considered as potential solid-state hydrogen

storage materials until the pioneering work by Bogdanovic et al.,^{16,17} demonstrating sodium aluminum hydride (sodium alanate, NaAlH_4) as a promising complex metal hydride for onboard hydrogen storage. NaAlH_4 offers a reasonable hydrogen storage capacity (~7.4 wt %) when decomposing in three steps with 3.7, 1.9, and 1.8 wt % release of hydrogen, respectively¹⁶



Received: March 14, 2012

Revised: May 8, 2012



The pure sodium alantes suffer from the limitations such as unfavorable thermodynamics (high temperature required to release hydrogen), slow kinetics of hydrogen desorption, and irreversibility. Results from previous research have demonstrated the improvement in the thermodynamics and kinetics of Na alanate by doping/catalyzing with Ti-based dopants^{16,17} and by preparing nanocrystalline NaAlH₄.^{18–20} However, the positive benefits of Ti-doped NaAlH₄ as well as nanosized NaAlH₄ have been offset by the considerable loss in the reversible storage capacity during the multiple de-/rehydrogenation cycles on account of the inevitable particle agglomeration driven by the segregation of the resulting Al domains.^{42,43} During the recent years, various other catalysts such as metals,^{13–15,21–25} rare-earth and transition-metal halides, and oxides^{26–41} have been employed to overcome these limitations. Nevertheless, the practical utilization of most of the rare-earth and transition-metal halides and oxides as dopants is limited by the generation of some inactive reaction byproducts, rendering the significant deterioration of practical hydrogen storage capacity. Moreover, for most of these catalysts, the underlying mechanisms concerning the formation of catalytic active species during the doping as well as cycling are not yet thoroughly understood. Therefore, there have been persistent efforts to explore new effective catalysts that can enhance the reaction kinetics and cyclic reversibility while maintaining the high hydrogen capacity. During the past decade, it has been recognized that a viable strategy to overcome these limitations involves combining the complex hydrides with small amounts of nanosized catalytic dopant. It is believed that the limited reversibility of the NaAlH₄ system, induced by long solid state diffusion paths due to macroscopic phase segregation, can be overcome by employing nanocatalytic additives.

Recently, it has been shown that various metal oxides such as transition-metal oxides as well as rare-earth oxides can improve the hydrogen sorption kinetics of Na alanate. It is reported that the addition of lanthanide oxide powders to Na alanate has triggered more hydrogen release than that with Ti halides.³⁶ However, the use of these powders has presented poor hydrogen sorption kinetics. The previous investigations have also revealed that Ti_{1.5}·6THF, TiN, and TiO₂^{40,44–46} nanoparticles are more effective in improving the hydrogen sorption properties of NaAlH₄ compared to that of TiCl₃ and rare-earth oxides. Nevertheless, the works presented by Lee et al.⁴⁶ and Pukazhselvan et al.⁴⁰ have reported contradictory results about the catalytic mechanism of TiO₂ nanopowders. Moreover, in our recent studies on Li alanate,⁶ it was found that Nb₂O₅ nanoparticles are superior to Cr₂O₃ in enhancing the kinetic and thermodynamic performance of LiAlH₄. Previous studies^{47–49} have also indicated the efficacy of Nb₂O₅ and Cr₂O₃ in improving the decomposition thermodynamics and kinetics of MgH₂. Motivated by the above findings, we have further extended the usage of oxide nanoparticles for NaAlH₄. In the present work, the relative efficiencies of Nb₂O₅, TiO₂, and Cr₂O₃ nanoparticles have been investigated by subjecting the doped samples to thermogravimetry (TG), differential scanning calorimetry (DSC), and isothermal volumetric measurements. On the basis of X-ray diffraction (XRD), X-ray photoelectron spectroscopy (XPS), Fourier transform infrared (FTIR), and FESEM-EDS analyses, the present study provides the pioneer-

ing results concerning the oxidation state and the local structure of Nb, Ti, and Cr species during the various steps of milling and cycling, contributing to the understanding of the reaction mechanism and the influence of the additives on the kinetics. Moreover, the kinetics of desorption reactions are analyzed qualitatively with regard to the rate-limiting processes by applying the various kinetic models.

EXPERIMENTAL SECTION

NaAlH₄ (hydrogen storage grade, ≥93% purity) was purchased from Sigma-Aldrich Co. The high purity nano-oxides Nb₂O₅, Cr₂O₃ (≥99%, 50–80 nm), and TiO₂ (≥99%, 15–20 nm) were provided by SINONANO Co., Ltd. (China). All the materials were used as received without any further purification. All material handlings (including weighing and loading) were performed in a high purity argon-filled glovebox, with low oxygen and water vapor contents of below 1 ppm. NaAlH₄ (typically 1–2 g) was mixed with various mole fractions of Nb₂O₅, TiO₂, and Cr₂O₃ nanosized powders and subsequently ball milled for 30 min by using a high-energy Spex 8000 Mixer/Mill. For comparison, undoped NaAlH₄ was also milled for 30 min. All the samples were loaded into the hardened steel vial under an argon atmosphere in a glovebox. Steel balls (1 and 3 g) were added with a ball to powder weight ratio of 15:1. The used mill was equipped with forced air cooling to permit the extended milling times as well as to prevent the heating of the vial during the ball-milling process.

Nonisothermal dehydrogenation performances were investigated by thermogravimetry (TG) and differential scanning calorimetry (DSC). The DSC and TG analyses were conducted by using NETZSCH STA 449C. All measurements were carried out under a flow (50 mL/min) of high purity argon (99.999%). The sample mass was typically 5 mg. Heating runs were performed at different rates (4, 7, and 10 °C min⁻¹) from 35 to 500 °C.

The isothermal de-/rehydrogenation kinetics were measured by using a pressure–composition–temperature (PCT) apparatus. The details of the apparatus are given in our previous reports.^{5,6,50} The apparatus can be operated up to the maximum pressure of 10 MPa and 600 °C. About 0.5 g of sample was loaded into the sample vessel. The isothermal dehydrogenation measurements for the undoped and doped samples were performed at 120 and 150 °C under a controlled vacuum atmosphere. Following the first complete dehydrogenation, the samples were subjected to rehydrogenation studies at 120 °C under 9.5 MPa for 3 h. Subsequently, the rehydrogenated samples were dehydrogenated at 150 °C.

The phase structure of the sample following the ball milling, dehydrogenation, and rehydrogenation was determined by a MXP21VAHF X-ray diffractometer (XRD with Cu K α radiation) at room temperature. XRD was done at a tube voltage of 40 kV and a tube current of 200 mA. The samples were covered with the paraffin film to prevent the oxidation during the XRD test.

X-ray photoelectron spectroscopy (XPS) experiments were performed in an ultra high vacuum (UHV) chamber with the base pressure of around 3×10^{-13} MPa, equipped with a Perkin-Elmer PHI-5300 XPS spectrometer. FTIR spectroscopy was performed by using an infrared spectrophotometer (NEXUS670). The spectral resolution was 4 cm⁻¹. Scans were done between 3000 and 200 cm⁻¹ under an argon atmosphere.

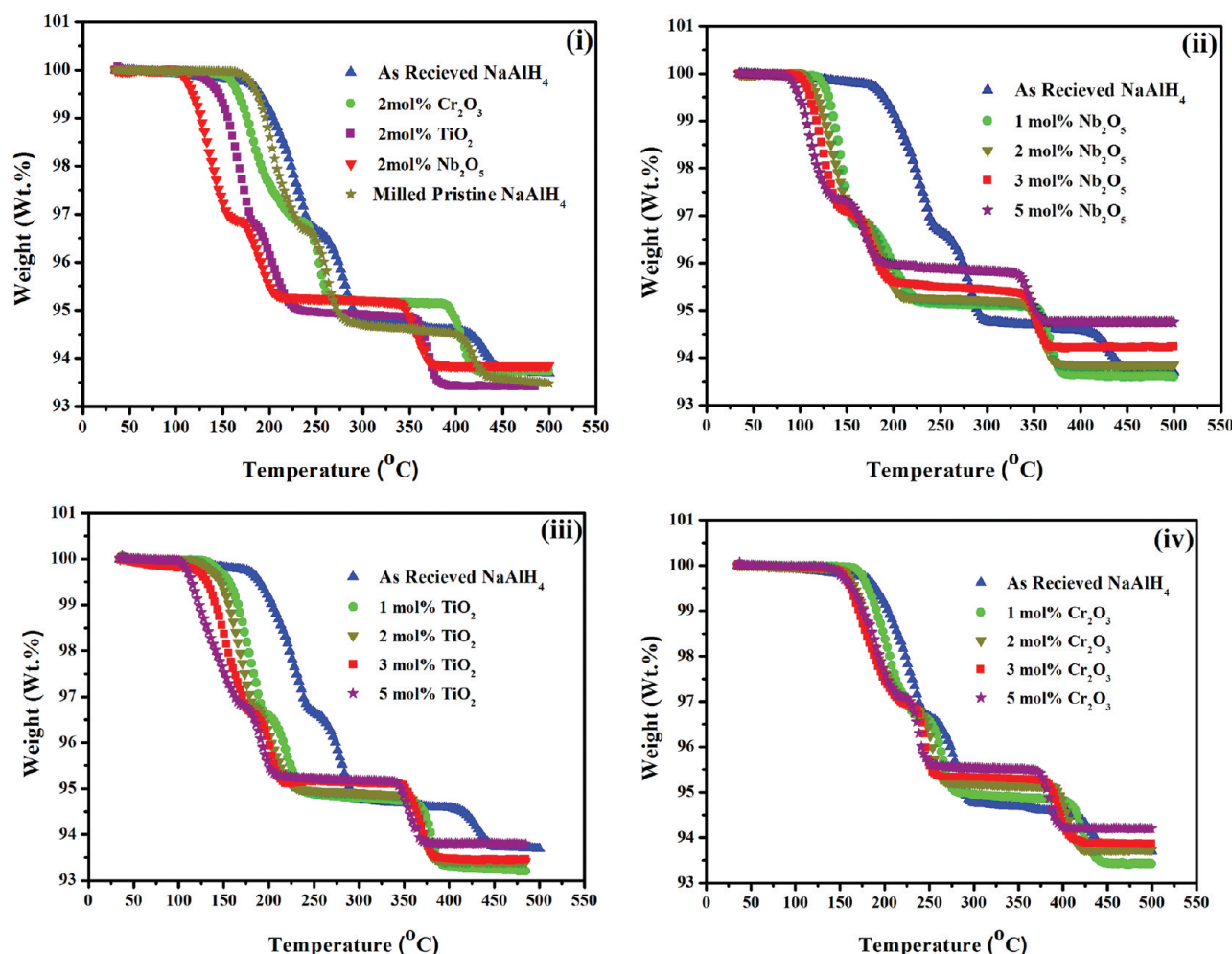


Figure 1. (i) Comparison of thermal desorption profiles of neat NaAlH_4 , milled NaAlH_4 , and NaAlH_4 doped with 2 mol % Nb_2O_5 , TiO_2 , and Cr_2O_3 nanoparticles and (ii), (iii), (iv) NaAlH_4 doped with 1 mol %, 2 mol %, 3 mol %, and 5 mol % Nb_2O_5 , TiO_2 , and Cr_2O_3 nanoparticles. The ramping rate is $4\text{ }^{\circ}\text{C min}^{-1}$.

As-received, doped, and dehydrogenated samples were examined by a field emission scanning electron microscope (FESEM-6301F) coupled with energy dispersive spectroscopy (EDS). As-received nano-oxide powders have been examined by a transmission electron microscope (JEM-2100F). Samples for the FESEM were transferred to the SEM chamber by means of a device maintaining an Ar overpressure.

RESULTS AND DISCUSSION

The TG profiles in Figure 1(i) depict the nonisothermal dehydrogenation performances of Na alanate undoped and doped with 2 mol % nano-oxide additives. The desorption curves clearly reveal that the use of nanometric Nb_2O_5 , TiO_2 , and Cr_2O_3 additions has rendered quite striking effects not only on the dehydrogenation characteristics of first and second steps but also on the third step. In the case of pristine NaAlH_4 , hydrogen release starts at $178\text{ }^{\circ}\text{C}$, and weight loss is about 5.2 wt % after heating to $290\text{ }^{\circ}\text{C}$. The third decomposition commences at $410\text{ }^{\circ}\text{C}$, and a hydrogen release capacity of 6.3 wt % is obtained below $450\text{ }^{\circ}\text{C}$. For the undoped milled Na alanate, the onset dehydrogenation temperature as well as dehydrogenation temperature range have lowered only by about $10\text{--}13\text{ }^{\circ}\text{C}$. The Nb_2O_5 and TiO_2 nanopowders have exhibited superior catalytic effects compared to that of Cr_2O_3

nanoadditives. The sample with Nb_2O_5 initiates to decompose at $100\text{ }^{\circ}\text{C}$ and terminates at $155\text{ }^{\circ}\text{C}$ for the first stage, while the sample containing TiO_2 starts to decompose at $120\text{ }^{\circ}\text{C}$ and concludes at $186\text{ }^{\circ}\text{C}$. Obviously, the first-stage decomposition temperature for samples with Nb_2O_5 and TiO_2 additives has reduced by 78 and $50\text{ }^{\circ}\text{C}$, respectively, compared to that of the pristine Na alanate. The second stage decomposition of $\text{NaAlH}_4\text{-Nb}_2\text{O}_5$ and $\text{NaAlH}_4\text{-TiO}_2$ terminates at about 90 and $70\text{ }^{\circ}\text{C}$ lower than that for pure NaAlH_4 . Further heating of $\text{NaAlH}_4\text{-Nb}_2\text{O}_5$ and $\text{NaAlH}_4\text{-TiO}_2$ samples leads to third decomposition (the decomposition of NaH according to eq 3), starting at about 340 and $355\text{ }^{\circ}\text{C}$, respectively, which is also 60 and $55\text{ }^{\circ}\text{C}$ lower than that of a pure NaAlH_4 sample. The onset of hydrogen desorption for 2 mol % Cr_2O_3 with added NaAlH_4 appeared around 151, 235, and $386\text{ }^{\circ}\text{C}$, respectively, which are 51, 57, and $46\text{ }^{\circ}\text{C}$ higher than the corresponding decomposition temperatures of samples with Nb_2O_5 addition. These results corroborate that the Nb_2O_5 nanoadditive is more efficient than TiO_2 as well as Cr_2O_3 nanoadditives. The dehydrogenation temperature range for the TiO_2 -doped sample, observed in the present work, is in good agreement with that reported by Lee et al.⁴⁶ for a sample of NaAlH_4 doped with 2 mol % TiO_2 nanopowder. Moreover, it is also noted that the desorption temperature range for NaAlH_4 with Nb_2O_5 , recorded in the present work, is smaller than that for NaAlH_4

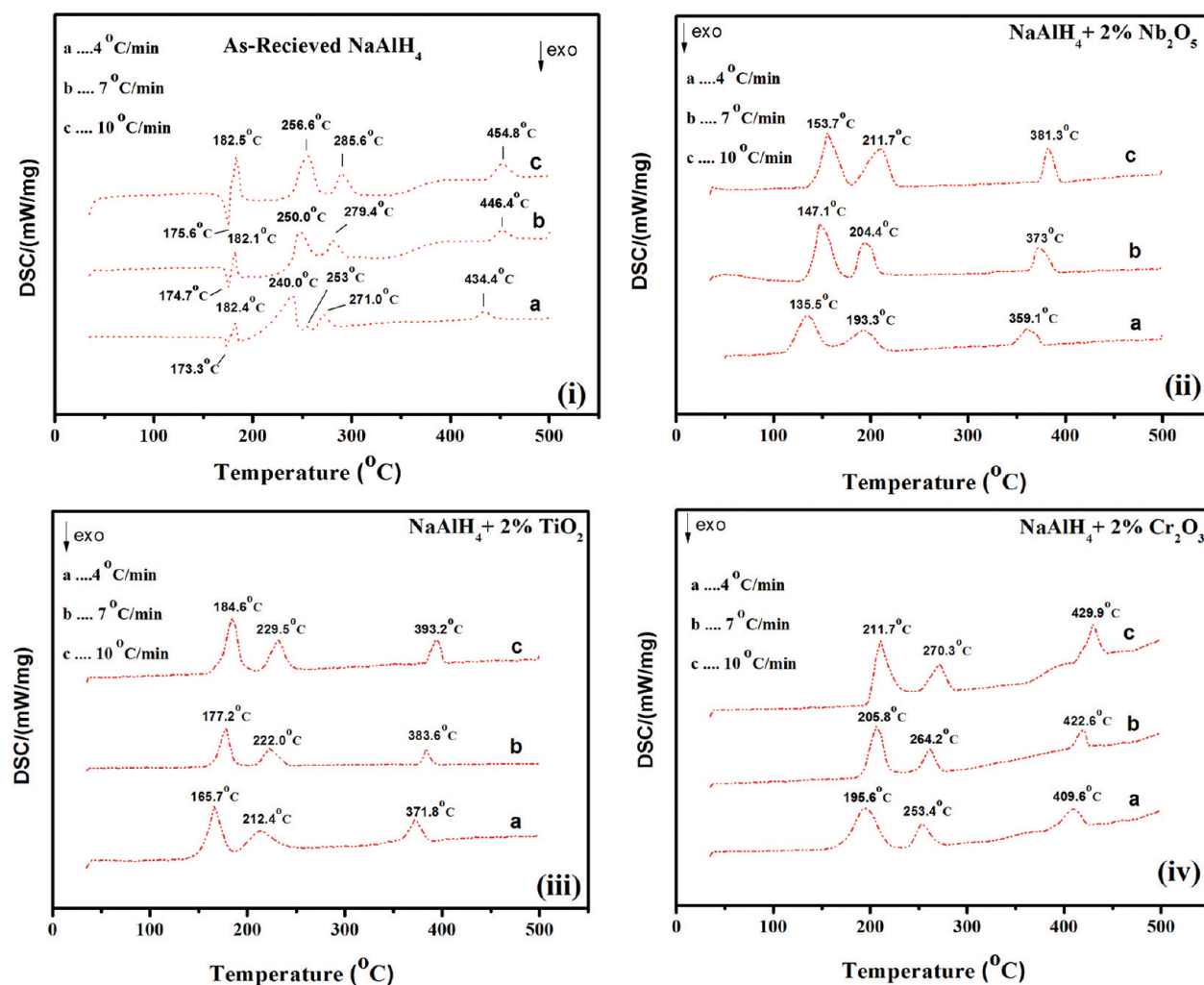


Figure 2. DSC profiles at various heating rates ($4, 7$, and $10\text{ }^{\circ}\text{C min}^{-1}$) for (i) pristine NaAlH_4 and (ii), (iii), and (iv) NaAlH_4 doped with 2 mol % Nb_2O_5 , TiO_2 , and Cr_2O_3 nanoparticles.

with various other metal oxide catalysts (TiO_2 , Sm_2O_3 , La_2O_3 , Gd_2O_3 , Nd_2O_3 , Pr_2O_3 , Ce_2O_3 , Eu_2O_3) reported previously in the literature.^{36,40,46}

The manometric desorption profiles in Figure 1(ii–iv) show the effects of various mole fractions of nanosized oxide additions on the hydrogen desorption temperatures and capacities of NaAlH_4 . The onset temperatures of hydrogen desorption for the milled 1, 2, 3, and 5 mol % Nb_2O_5 added NaAlH_4 composites appear around 116, 100, 93, and 82 °C, respectively, which are 62, 78, 84, and 95 °C lower than that of pure Na alanate. In particular, for the doped samples with 5 mol % Nb_2O_5 and TiO_2 nanoparticles, the dehydrogenation temperature ranges (first two stages) have lowered to 82–190 °C and 100–208 °C, respectively. On the contrary, the addition of increasing amounts of Cr_2O_3 nanoparticles to NaAlH_4 results in a progressive reduction of the onset temperature of NaAlH_4 by as much as 145 °C and 132 °C for the mixtures containing 3 and 5 mol % Cr_2O_3 , respectively. It implies that a smaller amount of Nb_2O_5 is required to decrease the dehydrating temperature onset of NaAlH_4 compared to that of TiO_2 as well as Cr_2O_3 . Moreover, a total of 4.5 and 3.9 wt % hydrogen is released below 200 °C for 2 mol % Nb_2O_5 and TiO_2 dopants, respectively. In contrast, only 2.4 and 0.9 wt % hydrogen is released above 200 °C for NaAlH_4 –2 mol % Cr_2O_3 and the pristine alanate samples,

respectively. Hence, the addition of Nb_2O_5 nanoparticles facilitates to generate more hydrogen below 200 °C. In addition, the total hydrogen release contents (first two stages) from 2 mol % Nb_2O_5 , TiO_2 , and Cr_2O_3 doped samples are around 4.8, 5, and 4.8 wt.%, in the temperature ranges of 100–210 °C, 120–230 °C, and 151–268 °C, respectively. It corroborates that a significant reduction in the decomposition temperature arising upon adding TiO_2 and Nb_2O_5 catalysts is achieved without much penalty of the practical capacity of materials. Moreover, the Na alanate with 2 mol % Nb_2O_5 and TiO_2 releases 4.8 and 5 wt % hydrogen, respectively, which is in contrast with the hydrogen capacity of Na alanate with TiCl_3 and TiO_2 additions reported previously.⁴⁶ Furthermore, these capacities are quite large compared to that of NaAlH_4 with lanthanide and other rare earth oxide catalysts.^{36,40} However, it is evident for all types of dopants that an increase of the doping amount shortens the desorption temperature range but with the cost of more loss of hydrogen capacity. The amount of H_2 (first two stages) released decreases from a high of about 5.1 and 4.9 wt % for 1 mol % TiO_2 and Nb_2O_5 dopants to a low of about 4.7 and 4.1 wt % for the mixtures containing 5 mol % TiO_2 and Nb_2O_5 , respectively. This reduction in hydrogen capacity is most likely due to an increasing weight penalty that occurs as the percentage of oxide additives in the mixture increases. By considering that a large amount of dopant is detrimental in

Table 1. Comparison of Activation Energies and Decomposition Enthalpies of Pure and Doped NaAlH₄

parameter	sample	way of determination	NaAlH ₄	NaAlH ₃	references
activation energy (kJ/mol)	Pristine NaAlH ₄	Kissinger Method	114.2, 132	156.8, 268	12,11
	Pristine NaAlH ₄	Isothermal	118.1	120.7	13
	Pristine NaAlH ₄	Kissinger Method	116.2	149.3	Present work
	With nano Nb ₂ O ₅	Kissinger Method	65.3	85.6	Present work
	With nano TiO ₂	Kissinger Method	73.5	101	Present work
	With nano Cr ₂ O ₃	Kissinger Method	98.9	119.1	Present work
	With CeCl ₃	Kissinger Method	80.8	97.2	12
	With CeAl ₄	Kissinger Method	80.9	98.9	12
	With TiCl ₃	Isothermal	80	97.5	13
	With Ti	Kissinger Method	77	-	40
	With TiO ₂	Kissinger Method	67	-	40
	With Ti/Ti _{1.3} 6THF	Kissinger Method	96.2	197.2	14
	With Ti/TiCl ₃	Kissinger Method	139.5	-	14
	With CeAl	Kissinger Method	72.3	98.9	8
	With LaCl ₃	Kissinger Method	86.4	96.1	9
	With La ₃ Al ₁₁	Kissinger Method	92.9	99.2	9
	With SmCl ₃	Kissinger Method	89	96.7	9
	With SmAl ₃	Kissinger Method	91.9	98.9	9
	With TiF ₃	Kissinger Method	98	130	11
	With SiO ₂	Kissinger Method	127	138	11
	With TiF ₃ + SiO ₂	Kissinger Method	99	122	11
decomposition enthalpy (kJ/mol)	Pristine NaAlH ₄	Experimental	38.7	49.6, 41.5	15,17
	Pristine NaAlH ₄	Theoretical	38.8, 34.5, 36.7	20.4, 23.8, 69.6	52,53
	Pristine NaAlH ₄	Experimental	39.9	48.5	Present work
	With nano Nb ₂ O ₅	Experimental	30.8	34.4	Present work
	With nano TiO ₂	Experimental	32.7	38.0	Present work
	With nano Cr ₂ O ₃	Experimental	37.1	44.5	Present work
	With Ti	Experimental	37, 34.9	47, 51.9	17,23
	With Ti + KH	Experimental	35.1	46.5	23

terms of gravimetric hydrogen density, 2 and 3 mol % doping amounts can be considered as a best compromise between the dehydrogenation rate and the hydrogen capacity.

The calorimetric profiles in Figure 2(i–iv) further verify the catalytic effect of oxide nanoadditives on the dehydrogenation reaction of NaAlH₄. Figure 2 illustrates the DSC results of NaAlH₄ undoped and doped with 2 mol % of each nano Nb₂O₅, TiO₂, and Cr₂O₃ within the temperature range of 35–500 °C at various heating ramps of 4, 7, and 10 °C min⁻¹, respectively. The pristine NaAlH₄, at 4 °C min⁻¹, exhibits one peak corresponding to an exothermic event and four peaks corresponding to endothermic events. The first exothermic peak corresponds to the interaction of NaAlH₄ with surface hydroxyl impurities, as reported for Li alanate in our previous reports.^{5,6} The second endothermic peak arises from the melting of NaAlH₄. The third process is assigned to the dehydrogenation of NaAlH₄ to Na₃AlH₆, i.e., eq 1. The fourth process may be attributed to a phase transition of α -Na₃AlH₆ to β -Na₃AlH₆.¹¹ The fifth and sixth endothermic peaks are assigned to the dehydrogenation of Na₃AlH₆ and NaH, as indicated by eqs 2 and 3, respectively. Obviously, the profiles at higher heating rates display the disappearance of the phase transition event. It is speculated that the peaks associated with desorption of NaAlH₄ and phase transition of Na₃AlH₆ overlap at higher heating rates, resulting in the disappearance of a Na₃AlH₆ phase transition event. In contrast with the calorimetric profiles of bare Na alanate, the features of all doped samples are strikingly different, displaying only three endothermic peaks. These three endothermic peaks, in Figure 2(ii–iv), correspond to three hydrogen desorption steps in

reactions 1, 2, and 3, respectively. It implies that NaAlH₄ decomposes at a much lower temperature without melting with nano-oxide catalysis. The resulting peak temperatures, measured in Figure 2(ii–iv), are quite small compared to that of pure and catalyzed Na alanate documented in the previous reports.^{11,15,23–25,31,36,45}

To comprehend the kinetics of H-sorption reactions arising upon the addition of oxide nanoadditives, the apparent activation energy corresponding to NaAlH₄, Na₃AlH₆, and NaH decompositions, for both undoped and doped NaAlH₄ composites, is estimated by the Kissinger method.⁵¹ The values of activation energy for the first and second dehydrogenation steps are summarized in Table 1. For comparison, the activation energies of NaAlH₄, undoped and doped with other additives, are also recapitulated in Table 1. The apparent activation energies, calculated for the pure alanate, are 116, 149, and 180 kJ/mol, for the first, second, and third decomposition steps, respectively. It is evident in Table 1 that the values of activation energy for the first and second steps for pure alanate (Table 1), acquired in the present work, compare favorably to that reported by Fan et al.¹² With the doping of TiO₂ nanoparticles, the activation energy has lowered to 73, 101, and 142 kJ/mol for NaAlH₄, Na₃AlH₆, and NaH relevant decompositions, respectively, which exhibits an enhancement in kinetics. Table 1 indicates that the value of activation energy with TiO₂, for the first step, is slightly higher than that reported with TiO₂⁴⁰ but lower than that for all other additives. The derived apparent activation energies corresponding to NaAlH₄, Na₃AlH₆, and NaH decompositions for the Na alanate, catalyzed with Nb₂O₅ nanoparticles, are 65, 85, and 131 kJ/

mol, respectively. It implies that Nb_2O_5 has induced a significant reduction in the activation energies of three stages compared to that of the undoped alanate sample. Table 1 clearly demonstrates that the values of activation energy with Nb_2O_5 are smaller than that reported for NaAlH_4 with all other additives. In addition, the DSC curves are analyzed by NETZSCH thermal analysis software. For the as-received sample, the reaction enthalpies of the first two decompositions are 39.9 ± 0.06 and 48.5 ± 0.04 kJ/mol, respectively. Table 1 also compares the desorption enthalpies determined in the present work to those of previously reported ones.^{15,17,23,52,53} The comparison suggests that the decomposition enthalpies of $\text{NaAlH}_4/\text{Nb}_2\text{O}_5$ (30.8 ± 0.11 and 34.4 ± 0.08 kJ/mol) and $\text{NaAlH}_4/\text{TiO}_2$ (32.7 ± 0.13 and 38 ± 0.1 kJ/mol) for the first two reaction steps are lower than those of $\text{NaAlH}_4/\text{Cr}_2\text{O}_3$ (37.1 ± 0.13 and 44.5 ± 0.09 kJ/mol) and as-received Li alanate, respectively. These results corroborate that the thermodynamics of Na alanate dehydrogenation is much affected by the addition of Nb_2O_5 and TiO_2 nanopowders. Therefore, it can be concluded that the addition of nano Nb_2O_5 and TiO_2 nanoparticles facilitates the hydrogen release with less energy consumption by the particle size reduction and crystal structure modification using high energy ball milling. In contrast, the higher values of enthalpies, found for the $\text{NaAlH}_4/\text{Cr}_2\text{O}_3$ mixture, account for its higher desorption temperatures compared to that of mixtures with Nb_2O_5 and TiO_2 nanoparticles.

The pronounced effect of oxide nanopowders in promoting the desorption kinetics of Na alanate is further demonstrated in isothermal volumetric measurements. Figure 3 presents the

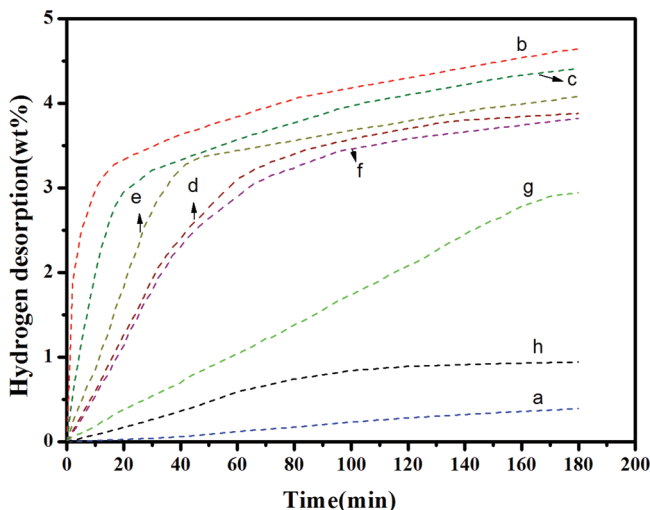


Figure 3. Comparison of the isothermal dehydrogenation curves for (a) as-received NaAlH_4 at 150°C , (b,e) $\text{NaAlH}_4 + 2 \text{ mol } \% \text{Nb}_2\text{O}_5$ at 150 and 120°C , (c,f) $\text{NaAlH}_4 + 2 \text{ mol } \% \text{TiO}_2$ at 150 and 120°C , (d,g) $\text{NaAlH}_4 + 2 \text{ mol } \% \text{Cr}_2\text{O}_3$ at 150 and 120°C , and (h) undoped milled NaAlH_4 .

dehydrogenation kinetics at 120 and 150°C for the samples with nano-oxide additives, respectively. For comparison, the dehydrogenation kinetics of the pure NaAlH_4 and undoped milled NaAlH_4 , decomposed at 150°C , is also included. The desorption rate is much slower for the pristine as well as undoped milled NaAlH_4 at 150°C . The desorption kinetics exhibit an enhancement after doping with Cr_2O_3 . However, the enhancements arising upon adding Nb_2O_5 and TiO_2 are more

significant. Within 180 min, the Cr_2O_3 -doped NaAlH_4 had only desorbed 3.9 and 2.9 wt % hydrogen at 150 and 120°C , respectively. The $\text{NaAlH}_4/\text{TiO}_2$ composite can release 4.4 and 3.8 wt % hydrogen in 180 min at 150 and 120°C , respectively. Under the same conditions, the Nb_2O_5 -doped sample has yielded 4.6 and 4.1 wt % of hydrogen. Moreover, the $\text{NaAlH}_4-\text{Nb}_2\text{O}_5$ sample has desorbed about 3 wt % hydrogen after 10 min at 150°C , which is higher than for $\text{NaAlH}_4/\text{TiO}_2$ (2 wt %) and much higher than for Cr_2O_3 -doped NaAlH_4 (0.6 wt %) at the same temperature. In contrast, 57 min is required for the undoped $\text{NaAlH}_4-\text{Cr}_2\text{O}_3$ sample to release 3 wt % hydrogen at 150°C . Evidently, the enhancements arising upon adding Nb_2O_5 are almost 1.4 times that of Cr_2O_3 additions. Moreover, it is clear that the Nb_2O_5 - and TiO_2 -doped samples have exhibited a nearly 11–12-fold increase in the average dehydrogenation rate than that of neat NaAlH_4 . It is also noticed that Nb_2O_5 - and TiO_2 -doped samples have exhibited the much faster kinetics compared to that of NaAlH_4 with various catalysts reported in the literature.^{11,15,19,23,27,35,39} Furthermore, the enhancements arising upon adding Nb_2O_5 and TiO_2 are superior to that reported previously with TiO_2 and other rare earth oxide catalysts.^{36,40,46}

For analysis of the rate-limiting processes during decomposition reactions, a qualitative approach is adopted by comparing the measured reaction kinetics with calculated values of known rate-limiting processes. The kinetic curves can be formulated as equations relating the transformed phase fraction to time. Thus, the kinetic rate-limiting step can be deduced, if a good fit of experimental data with the respective analytical equation can be obtained. Many solid-state reaction mechanism models have been proposed including the diffusion, the geometrical contraction, the nucleation, and the reaction order models based on the different geometry of the particles and the different driving forces. Table S1 (Supporting Information) summarizes some theoretical kinetic equations^{1,5,6,54,55} related to different rate-limiting steps. In these equations, α is transformed to a fraction in time t with the reaction constant k . All the models, listed in Table S1 (Supporting Information), have been applied to the measurements achieved at 120 and 150°C for Nb_2O_5 - and TiO_2 -doped samples. The results are presented in Figures 4 and 5. It is evident that different mechanisms are controlling the rates at different desorption temperatures except for the second dehydrogenation step of the Nb_2O_5 dopant. In Figures 4(b–d) and 5(a,b), the best correlation coefficient values correspond to the A2 and A3 models. These types of models describe the two- or three-dimensional growth of existing nuclei by the Avrami–Erofeev approach. Nucleation occurs randomly in the bulk of material, and growth can be controlled by an interface reaction leading to a constant interface velocity.^{6,54,55} For the Nb_2O_5 sample at 150°C , the kinetic analysis has revealed the best fit for the dehydrogenation as the reaction mechanism is based on the R2 model (Figure 4(a)). It implies a phase-boundary controlled reaction, in which nucleation occurs virtually instantaneously and desorption kinetics is controlled by the interface mobility of transformed phase along the two- or three-dimensional network of grain boundaries. The R2 model suggests that nucleation takes place rapidly at the surface of the particle, and growth continues from the surface into the bulk. The main speculation in this model is that this initial nucleation on the surface is fast compared with the overall growth kinetics and the nucleation zone is thin compared with the particle diameter.^{54,55} In Figure 5(c), the desorption for the

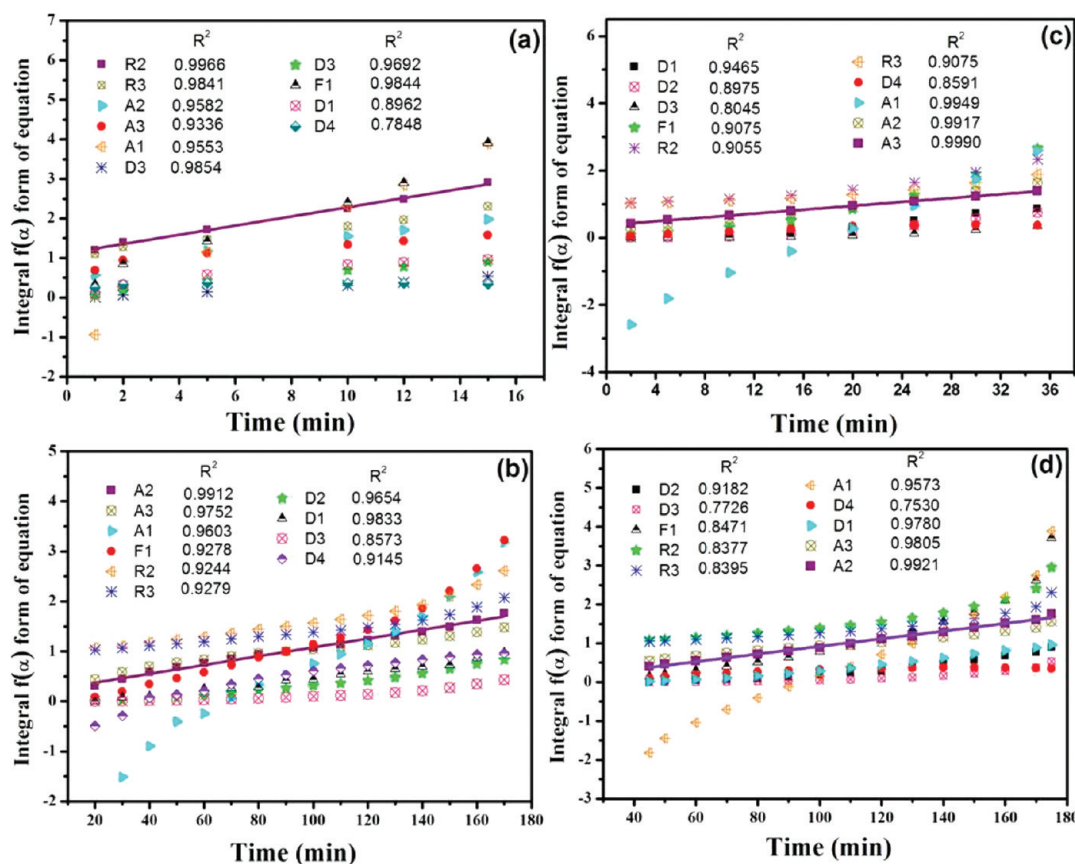


Figure 4. Curves of different kinetic models applied to the isothermal dehydrogenation of $\text{NaAlH}_4 + 2 \text{ mol } \% \text{Nb}_2\text{O}_5$ at (a) 150 °C (first step), (b) 150 °C (second step), (c) 120 °C (first step), and (d) 120 °C (second step). Illustration of kinetic models is given in Table S1 of the Supporting Information.

TiO₂-doped sample, at 120 °C, follows the Mampel unimolecular law formulated through random nucleation. In this approach, the hydrogen desorption is controlled by a slow, random nucleation process, and growth of a new phase begins randomly in the bulk and at the surface. Moreover, two-dimensional growth of randomly placed product nuclei in the form of edge-shaped planar circular discs proceeds homogeneously throughout the sample with the sample size remaining much greater than any individual transformed region.^{5,6,54,55} Moreover, it is found in Figures 4(c), 5(a), and 5(c) that for some models the differences in fitting quality are generally small, and at these temperatures it seems that the kinetics is driven by several mechanisms. Nevertheless, the appropriate model has been chosen giving the best correlation coefficient value among all the models.

With the aim to structurally elucidate the catalytic mechanism of oxide nanoparticles, XRD measurements of the doped composites, before and after being subjected to dehydrogenation at different temperatures, are displayed in Figures 6–8. The powder XRD patterns of as-received Na alanate and nanosized oxide additives are presented in Figure S1 (Supporting Information). The crystallite size is estimated by using the Scherrer equation. The initial crystallite sizes of nano Nb₂O₅, Cr₂O₃, and TiO₂ are determined to be 32, 40, and 12 nm, respectively. Figures 6 and 7 present the evolution of the XRD patterns of the $\text{NaAlH}_4-\text{Nb}_2\text{O}_5$ and $\text{NaAlH}_4-\text{Cr}_2\text{O}_3$ samples upon ball-milling and heating to different temperatures, successively. It is clear that the Nb₂O₅ and Cr₂O₃ phases can be detected in the XRD pattern of the as-milled materials.

It suggests that the Nb₂O₅ and Cr₂O₃ nanocrystalline particles remain stable with the NaAlH₄ matrix during ball-milling under the high-energy impact mode. In addition, the diffraction peaks are broadened, and their intensities are lowered, signifying the decrease in particle size and crystallite size and the formation of a large number of defects in the ball-milled composites. Figures 6(b) and 7(b) characterize the NaH and Al phases in the XRD patterns of the $\text{NaAlH}_4-\text{Nb}_2\text{O}_5$ and $\text{NaAlH}_4-\text{Cr}_2\text{O}_3$ samples after dehydrogenation at 210 and 270 °C, respectively. Figure 6a,b clearly depicts that the Nb₂O₅-doped sample, at the beginning, consists mainly of Nb₂O₅ and changes significantly during the heating and desorption process. It is evident that the heating of the sample up to 200 °C has induced the disappearance of crystalline Nb₂O₅, coupled to a parallel growth of new reduced niobium species with different oxidation states similar to NbO₂ (+4) and NbO/NbH (+2, +1). In contrast, the diffraction lines for Cr₂O₃ are still identified even after dehydrogenation, suggesting that Cr₂O₃ also remains stable during dehydrogenation [Figure 7(a,b)]. Figures 6c and 7c present the evolution of the XRD patterns of the Nb₂O₅- and Cr₂O₃-doped NaAlH₄ composite upon heating to 370 and 430 °C, respectively. It is obvious that the NaH phase has disappeared with the evolution of the Na phase, suggesting that hydrogen release is owing to decomposition of NaH as indicated in eq 3. Moreover, liberated hydrogen induces a further reduction of the niobium oxide when a steady state is reached, consisting mainly of phases with the oxidation states rich in +1(NbH) and +2(NbO) [Figure 6(c)].

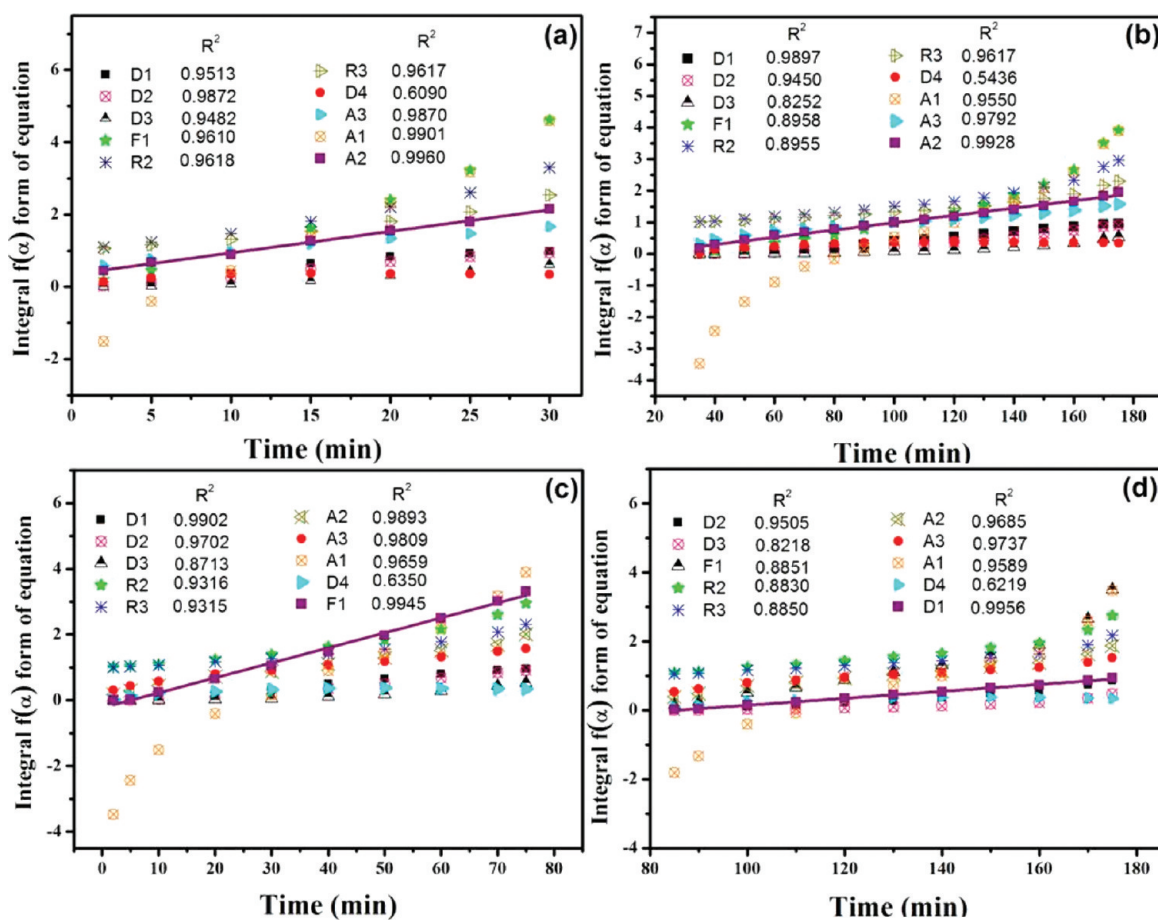


Figure 5. Curves of different kinetic models applied to the isothermal dehydrogenation of $\text{NaAlH}_4 + 2 \text{ mol } \% \text{ TiO}_2$ at (a) 150 °C (first step), (b) 150 °C (second step), (c) 120 °C (first step), and (d) 120 °C (second step). Illustration of kinetic models is given in Table S1 of the Supporting Information.

To comprehend the catalytic mechanism of TiO_2 nanoparticles, XRD measurements of the TiO_2 -doped NaAlH_4 sample, before and after being subjected to the dehydrogenation at different temperatures, are displayed in Figure 8. It is

evident that no indications are obtained from XRD regarding the Ti -based phases in both as-milled and cycled samples. This phenomenon may be ascribed to the high dispersion, the low content of the additive, and the nanocrystalline/amorphous

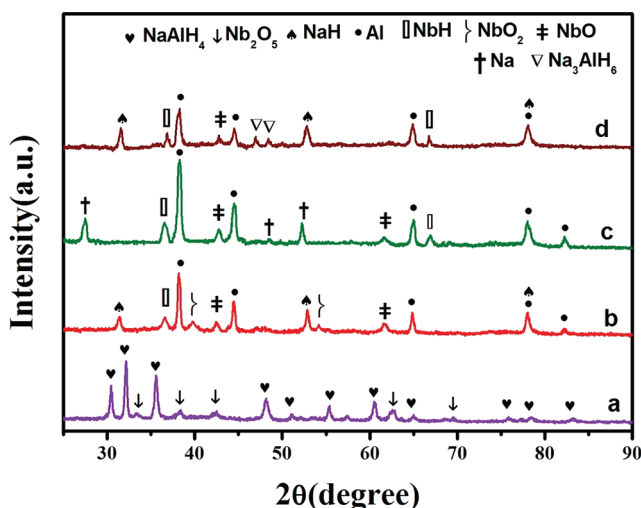


Figure 6. XRD patterns for the $\text{NaAlH}_4 - 3 \text{ mol } \% \text{ Nb}_2\text{O}_5$ composite at different states: (a) before dehydrogenation; (b) after dehydrogenation at 210 °C; (c) after dehydrogenation at 370 °C; (d) after third isothermal dehydrogenation at 150 °C for 3 h.

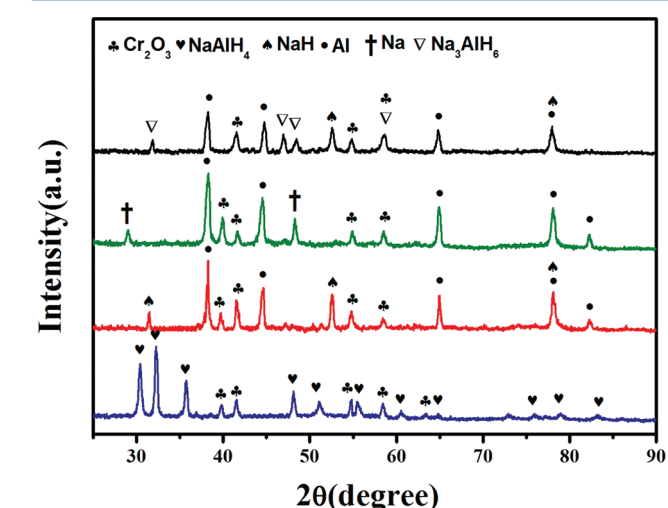


Figure 7. XRD patterns for the $\text{NaAlH}_4 - 3 \text{ mol } \% \text{ Cr}_2\text{O}_3$ composite at different states: (a) before dehydrogenation; (b) after dehydrogenation at 270 °C; (c) after dehydrogenation at 430 °C; (d) after third isothermal dehydrogenation at 150 °C for 3 h.

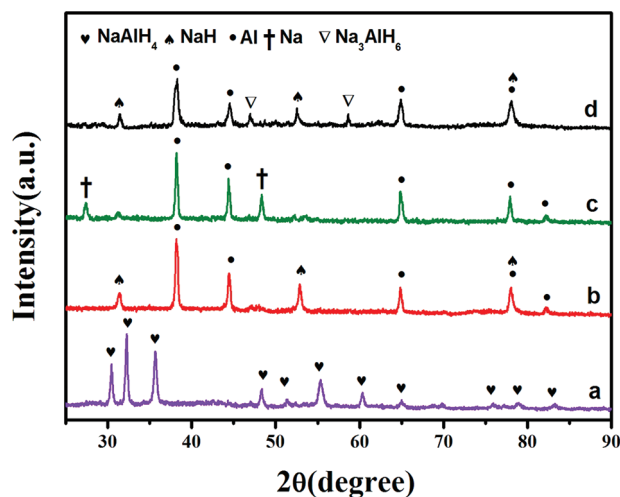


Figure 8. XRD patterns for the NaAlH_4 -3 mol % TiO_2 composite at different states: (a) before dehydrogenation; (b) after dehydrogenation at $220\text{ }^\circ\text{C}$; (c) after dehydrogenation at $390\text{ }^\circ\text{C}$; (d) after third isothermal dehydrogenation at $150\text{ }^\circ\text{C}$ for 3 h.

character of the Ti-based active phases. To obtain information about the chemical state and the local structure of the Ti-containing phase, XPS analysis on the milled samples of $\text{NaAlH}_4 + 3$ mol % TiO_2 has been performed before and after hydrogen cycling. Figure 9a shows the comparison of the surface chemical composition of the analyzed sample with the presentation of Ti 2p photoelectron peaks. The original milled sample has exhibited the fully oxidized Ti(IV) as the majority phase at the surface. The samples before cycling consist mainly of twin peaks of TiO_2 at 458.3 and 464.7 eV,⁵⁸ respectively. It indicates that TiO_2 nanocrystalline particles/clusters are present with the alanate matrix after ball milling. The Ti species are clearly reduced upon heating with the metallic Ti. The sample after complete dehydrogenation shows species similar to Ti (453.2 eV), TiO (454.6 eV), and Ti_2O_3 (462.0 eV).⁵⁶ It implies that the TiO_2 additive during desorption leads to a final state which is mainly a mixture of $\text{Ti(III)}(\text{Ti}_2\text{O}_3)$, $\text{Ti(II)}(\text{TiO})$, and Ti phases. The formation of reduced Ti species during the first desorption of milled MgH_2 with TiO_2 additive has been also previously reported by Croston et al.⁴⁷ Obviously, the Ti species are not further detected on the surface after the third cycle, indicating a migration of Ti species into the bulk upon cycling. This result shows that the highly dispersed reduced Ti and Ti-oxide active species may play their main role at the bulk phase boundaries during cycling where it may limit the grain growth of the formed phases, increasing the interfacial area and improving the kinetics in both discharging and recharging processes. These results are in good agreement with that reported for the TiO_2 -doped NaAlH_4 sample by Pukazhselvan et al.,⁴⁰ ascribing the enhanced catalytic activity of TiO_2 to its reduction. Moreover, it is speculated that once the active species are formed during first desorption the oxidation state and local structure of the Ti-based additive remain almost constant.

To further analyze the milling and cycling process, the chemical characterization of the Nb- and Cr-based additives has been also investigated by XPS in the milled $\text{NaAlH}_4 + 3$ mol % Nb_2O_5 and $\text{NaAlH}_4 + 3$ mol % Cr_2O_3 samples before and after hydrogen cycling. Figure 8b depicts the Nb 3d photoelectron peak region for the as-prepared sample compared to the desorbed and cycled samples. Figure 8b indicates the presence

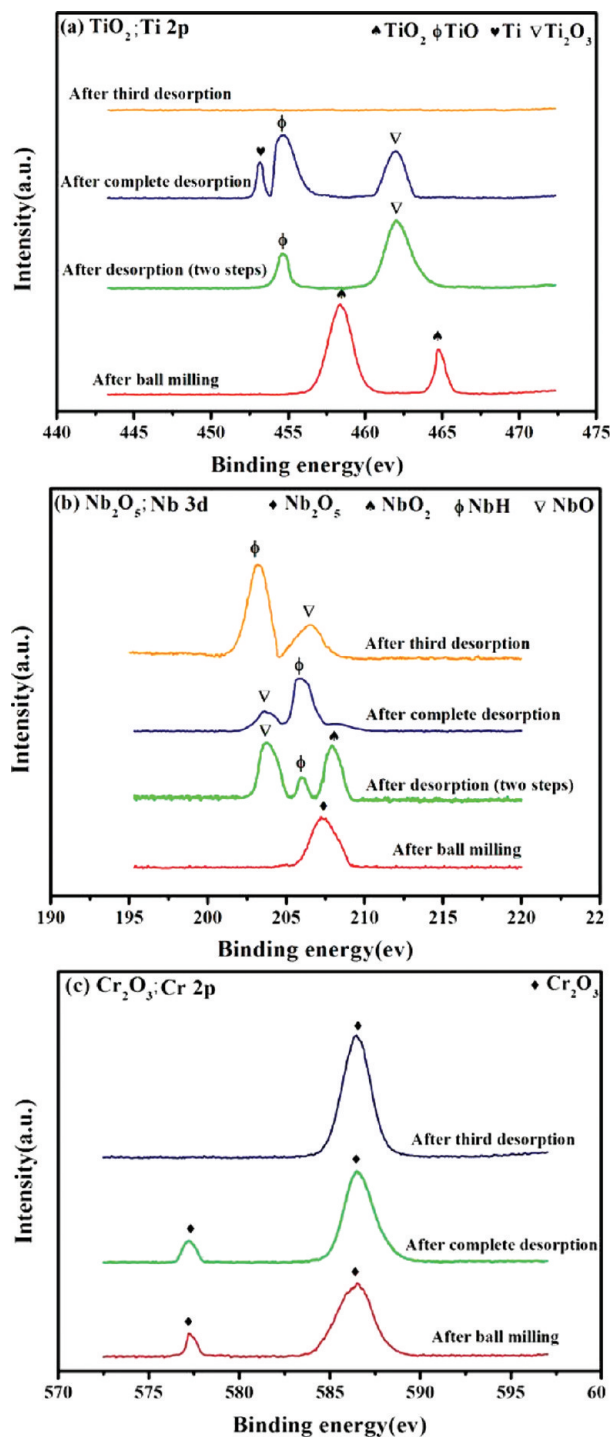


Figure 9. Narrow scan XPS. (a) Ti 2p spectra for 3 mol % TiO_2 -doped NaAlH_4 composite, (b) Nb 3d spectra for 3 mol % Nb_2O_5 -doped NaAlH_4 composite, and (c) Cr 2p spectra for 3 mol % Cr_2O_3 -doped NaAlH_4 composite before dehydrogenation, after dehydrogenation, and after the 3rd isothermal dehydrogenation.

of the Nb catalyst (207.2 eV) at the surface.^{6,56} The sample after first complete heating displays the contributions similar to NbO (203.7) and NbH (205.9 eV) species.^{6,56} All the changes that take place during the first desorption persist also during the next cycling. This is consistent with the results obtained from XRD. During the first hydrogen desorption, the reduction of Nb_2O_5 commences, and the originating products disperse in the sample and emerge to the surface. Figure 8c presents the Cr

2p photoelectron peaks for the as-milled, dehydrogenated, and cycled samples. All peaks at 577.1 and 586.4 eV before and after cycling correspond to Cr in Cr_2O_3 .⁵⁶ These results coincide with that of XRD, indicating that Cr_2O_3 is not dissolved or reduced before and after hydrogen cycling unlikely to TiO_2 and Nb_2O_5 . This observation is rather curious since Nb_2O_5 and Cr_2O_3 share the same valence of the O anion. Moreover, it has been suggested that transition metals can be reduced to their lower oxidation state by high temperatures under the hydrogen atmosphere. However, Cr_2O_3 is a thermodynamically more stable compound as compared to Nb_2O_5 ,⁴⁸ which is probably the reason for the stability of Cr_2O_3 during milling and cycling.

IR spectra of pristine and as-milled doped samples are shown in Figure 10. IR spectroscopy has been complementarily

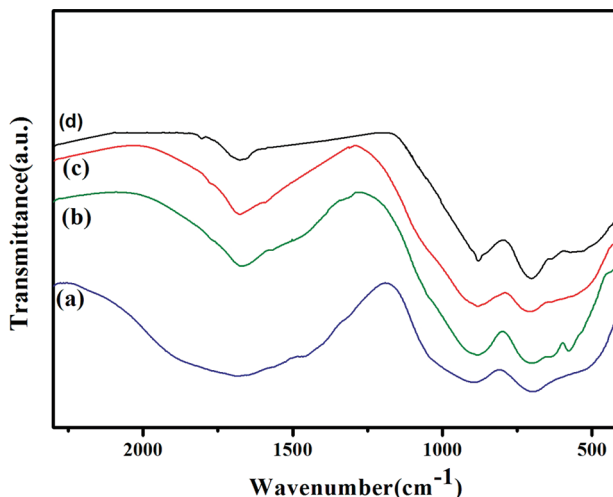


Figure 10. FTIR spectra of (a) as-received NaAlH_4 , (b) 3 mol % Nb_2O_5 -doped NaAlH_4 after ball milling, (c) 3 mol % TiO_2 -doped NaAlH_4 after ball milling, and (d) 3 mol % Cr_2O_3 -doped NaAlH_4 after ball milling.

performed to study the influence of oxide nanoparticles on the NaAlH_4 vibrational spectrum during milling. Active infrared vibrations of the Al–H bond of NaAlH_4 are found in two regions: Al–H stretching mode (1670 cm^{-1}) and H–Al–H bending modes (900 and 690 cm^{-1}).³³ With regard to Na_3AlH_6 ,⁵⁷ it also exhibits two regions of active infrared vibration: Al–H stretching modes (1440 and 1290 cm^{-1}) and H–Al–H bending modes (930 , 842 , and 690 cm^{-1}). For the as-received NaAlH_4 the broad band, centered at 1654 cm^{-1} , is observed [Figure 10(a)]. This can be attributed to the Al–H stretching frequency of NaAlH_4 . H–Al–H bending frequencies are observed at 896 and 694 cm^{-1} . With doping, similar stretching and bending vibration frequencies are observed. All three bands are still of NaAlH_4 , and no band of Na_3AlH_6 is found. However, it is evident in Table 2 that for doped alanates the Al–H stretching as well as bending modes are shifted slightly to lower and higher frequencies (2 – 23 cm^{-1}). This shift is presumably attributed to the anisotropic cell contraction and expansion caused by the low and high pressures reached during the milling process, resulting in the slight modification of the sodium coordination of the $[\text{AlH}_4]^-$ units.³³

Further study indicates that the catalytic enhancement arising upon adding TiO_2 , Nb_2O_5 , and Cr_2O_3 persists well in the dehydrogenation/rehydrogenation cycles. Figure S4 (Supporting Information) brings out the results of first rehydrogenation.

Table 2. Infrared Frequencies of Pure and Doped NaAlH_4 at Room Temperature

sample	H–Al–H bending (cm^{-1})	Al–H stretching (cm^{-1})	ref
Pure NaAlH_4	690	1670	33
	900		
Pure NaAlH_4	866	1694	31
	694	1654	Present work
Nb_2O_5 doped	896		
	696	1666	Present work
TiO_2 doped	883		
	703	1677	Present work
Cr_2O_3 doped	881		
	698	1670	Present work
	880		

The variations in hydrogen storage capacity and desorption kinetics during cycling of the doped samples are displayed in Figure 11. NaAlH_4 with Cr_2O_3 exhibits a rapid decrease in storage capacity, from about 3.9 wt % to about 3.4 wt % (in 3 h) in three cycles. On the other hand, NaAlH_4 with TiO_2 exhibits the least degradation, losing only 0.1 wt % during three cycles. This result is superior to that reported for NaAlH_4 with TiO_2 by Lee et al.⁴⁶ (4.6 wt % in 4 h for the first cycle to 4.3 wt % in 4 h for the third cycle). Moreover, the NaAlH_4 – Nb_2O_5 sample has also displayed the well-maintained kinetics and only a slight capacity loss as compared to the performance in the first cycle. It deteriorates from 4.6 wt % in 3 h (first dehydrogenation) to 4.4 wt % in 3 h (second dehydrogenation) and 4.3 wt % in 3 h (third dehydrogenation). We believe that the larger particle size and agglomeration of the catalytic species are essential considerations for deterioration of the cyclic capacity of Cr_2O_3 nanoparticles. The enhanced catalytic performance for TiO_2 and Nb_2O_5 nanoparticles may be ascribed to their smaller particle size and high dispersion. Moreover, the XPS results for TiO_2 have indicated that highly dispersed reduced Ti and Ti-oxide active species migrate to the bulk phase boundaries during cycling where it may limit the grain growth of formed phases, thus enhancing kinetics in both discharging and recharging processes by increasing the interfacial area. The XRD profiles of all doped samples following the third cycle, shown in Figures 6d, 7d, and 8d, indicate that capacity loss is mainly attributed to the incomplete decomposition of the intermediate Na_3AlH_6 phase. Evidently, the presence of more Na_3AlH_6 peaks for the Cr_2O_3 dopant accounts for its reduced cyclic capacity.

To further reveal the catalytic mechanism of oxide nanoadditives for the improvement of hydrogen sorption properties of NaAlH_4 , we finally resort to the microstructural analysis of the doped samples. Figure S2 (Supporting Information) depicts the TEM images of as-received metal oxide nanopowders. The images testify that the particle size of TiO_2 nanoparticles is about 20 nm, while for Nb_2O_5 and Cr_2O_3 nanopowders it is larger than 50 nm. Figure S3 (Supporting Information) indicates the FESEM results for pristine as well as undoped milled NaAlH_4 . Figure S3a (Supporting Information) indicates that prior to ball milling the pure NaAlH_4 exhibits irregular flaky-shaped particles with a mean particle size of more than 30 μm . The undoped milled NaAlH_4 sample has not

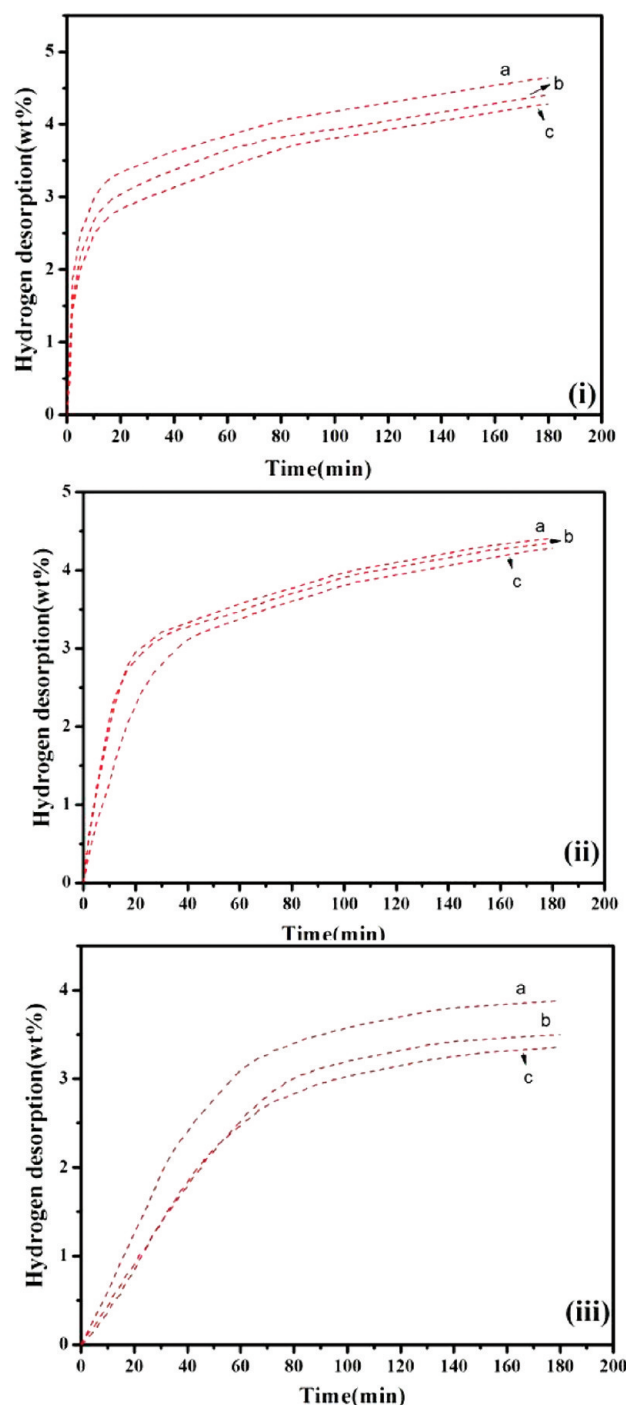


Figure 11. Comparison of the dehydriding curves at 150 °C for (i) 3 mol % Nb₂O₅-doped NaAlH₄, (ii) 3 mol % TiO₂-doped NaAlH₄, and (iii) 3 mol % Cr₂O₃-doped NaAlH₄ samples during the first three cycles.

exhibited an appreciable decrease in particle size [Figure S3b, Supporting Information]. Figure 12(a)–(f) presents the representative FESEM micrographs exhibiting the particle size and morphology of NaAlH₄ with Nb₂O₅, TiO₂, and Cr₂O₃ nanoparticles before and after hydrogen cycling. Figure 12(a)–(c) brings out the microstructural features of NaAlH₄ mechanically ball-milled with 3 mol % Nb₂O₅, TiO₂, and Cr₂O₃ nanoparticles. Remarkably, the nature of the dopant has exhibited an evident influence on the particle size distribution reached after the milling process. The FESEM analysis carried

out on the cross-section of doped samples has revealed the higher refinement induced by Nb₂O₅ and TiO₂ nanoparticles compared to that of Cr₂O₃ nanoparticles. The bright specks on the surface of hydride correspond to particles of Nb₂O₅, TiO₂, and Cr₂O₃. The size of most of the particles is less than 5 μm for the samples with Nb₂O₅ and TiO₂ dopants, indicating the significant diminution of particle size compared to that of undoped as well as Cr₂O₃-doped samples. It is conspicuous that TiO₂ and Nb₂O₅ nanoparticles are embedded heterogeneously in the hydride matrix, rendering the substantial surface modifications exhibiting many deformed and disordered surface regions (inset of Figure 12(a),(b)). On the contrary, the sample with Cr₂O₃ exhibits extensive agglomeration of Cr₂O₃ nanoparticles. The hardness of Nb₂O₅, TiO₂, and Cr₂O₃ is much higher than that of NaAlH₄. Nevertheless, Nb₂O₅ and TiO₂ are known for their good lubricant and dispersive properties that inhibit the agglomeration and cold welding of hydride particles and thereby facilitate the refinement of matrix particles during milling. The fraction of embedded Nb₂O₅ and TiO₂ nanoparticles will enhance the hardness and brittleness of hydride particles that will ultimately shift the balance between fracturing and agglomeration to smaller particle sizes. Moreover, it is evident in the inset of Figure 12(a),(b) that the Nb₂O₅ nanoparticles have produced more deformed and disordered surface regions around them, exhibiting many surface defects compared to that for TiO₂ nanoparticles. This phenomenon is probably imputed to a slightly higher hardness of Nb₂O₅ (7 Mohs) than that of TiO₂ (6 Mohs). Figure 12(d)–(f) brings out the microstructural features of the doped materials after the third dehydrogenation. The generation of small pores, observed at the matrix surface as well as between the aggregates of the primary particles, is attributed to the repeated volume shrinkage and expansion during sorption cycles. Moreover, the segregation of Al and LiH along with catalyst particles is much more in the Cr₂O₃ sample compared to that with Nb₂O₅ and TiO₂. Figure 13(a)–(f) is the surface EDS spectra collected at positions circled in Figure 12(a)–(f). Although the exact quantitative analysis is not available owing to the contribution from the NaAlH₄ matrix surrounding the dopant and the possible oxidation of the sample in its handling during the sample preparation, nonetheless, it can be confirmed that the particles in the areas, circled in Figure 12(a)–(f), are comprised of Na, Al, Nb, Ti, Cr, and O. In addition, the statistical analysis of EDS measurements for the undoped and cycled samples over many places demonstrates that the variations of Nb and Ti contents are large compared to that of Cr contents. Concomitant with XRD and XPS results, a change in peak positions of Nb/Ti following cycling corroborates that Nb₂O₅ and TiO₂ have reduced during cycling.

The above experimental results corroborate that the Nb₂O₅ and TiO₂ nanopowders profoundly affect the reaction kinetics and the sorption properties of Na alanate. The factors such as the larger reduction in the crystallite size of nanosized Nb₂O₅- and TiO₂-doped composites compared to that with nanosized Cr₂O₃ may account for their superior hydrogen sorption performance. The larger particle size and agglomeration for a sample with Cr₂O₃ limit the hydrogen desorption performance due to diffusion inhibition and passivation effects. The results of the present investigation also reveal that the addition of Nb₂O₅ and TiO₂ nanopowders can induce the generation of surface defects by rendering a substantial refinement of powder particles during the high-energy milling, which is expected to further ameliorate the kinetics as well as the hydrogen sorption

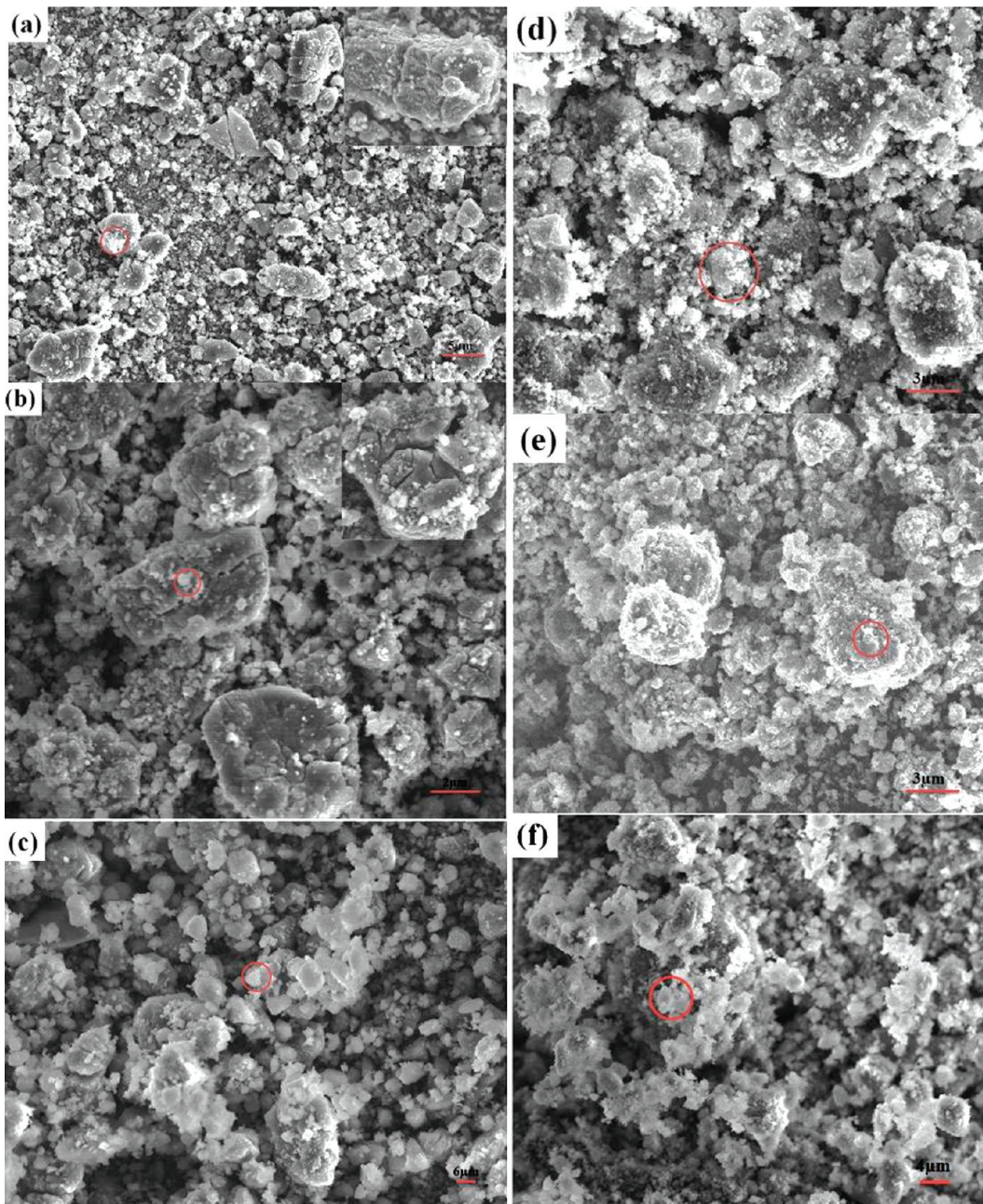


Figure 12. Field emission scanning electron microscopy (FESEM) images of (a) $\text{NaAlH}_4 + 3 \text{ mol } \% \text{Nb}_2\text{O}_5$ after ball milling, (b) $\text{NaAlH}_4 + 3 \text{ mol } \% \text{TiO}_2$ after ball milling, (c) $\text{NaAlH}_4 + 3 \text{ mol } \% \text{Cr}_2\text{O}_3$ after ball milling, (d) $\text{NaAlH}_4 + 3 \text{ mol } \% \text{Nb}_2\text{O}_5$ after dehydrogenation, (e) $\text{NaAlH}_4 + 3 \text{ mol } \% \text{TiO}_2$ after dehydrogenation, and (f) $\text{NaAlH}_4 + 3 \text{ mol } \% \text{Cr}_2\text{O}_3$ after dehydrogenation.

capability of Na alanate. It is documented in our previous works that hydrogen desorption/absorption is closely associated with surface defects and smaller particle sizes.^{5,6,50} First, the refined particle size renders the diffusion paths for hydrogen within the solid phase much shorter. Second, the relative surface area is much larger, and therefore more active surface sites are available for the gas–solid reaction. The reduced values of enthalpies, acquired in the present work for the doped samples, may also be ascribed to the small grain size and large number of defects which can also upset the order in the alanate crystal structure and enable hydrogen to desorb more easily. As the energies of both reactants and products change, going from bulk materials to nanosized particles, the reaction thermodynamics will be affected by the size of the grains.^{5,6} However, the

kinetic enhancements arising upon adding Nb_2O_5 and TiO_2 nanoparticles are not solely ascribed to the particle size diminution. Since Nb_2O_5 and TiO_2 are reduced during the heating, therefore, it is expected that partially reduced Nb and Ti species with a wide range of valence states may play a major role in improving the dehydrating/rehydrating property. Moreover, the reduction of Nb_2O_5 and TiO_2 during heating can also alter the thermodynamics of the reactions by lowering the enthalpy of the dehydrogenation reaction. Generally, for transition-metal-based catalysts, the main catalytic role is reported to be played by the transition metal ions and their ability to form hydrogen bonds with various stoichiometries. Therefore, we propose that hydrogen desorption/adsorption originates from oxygen vacancies on transition metal oxide

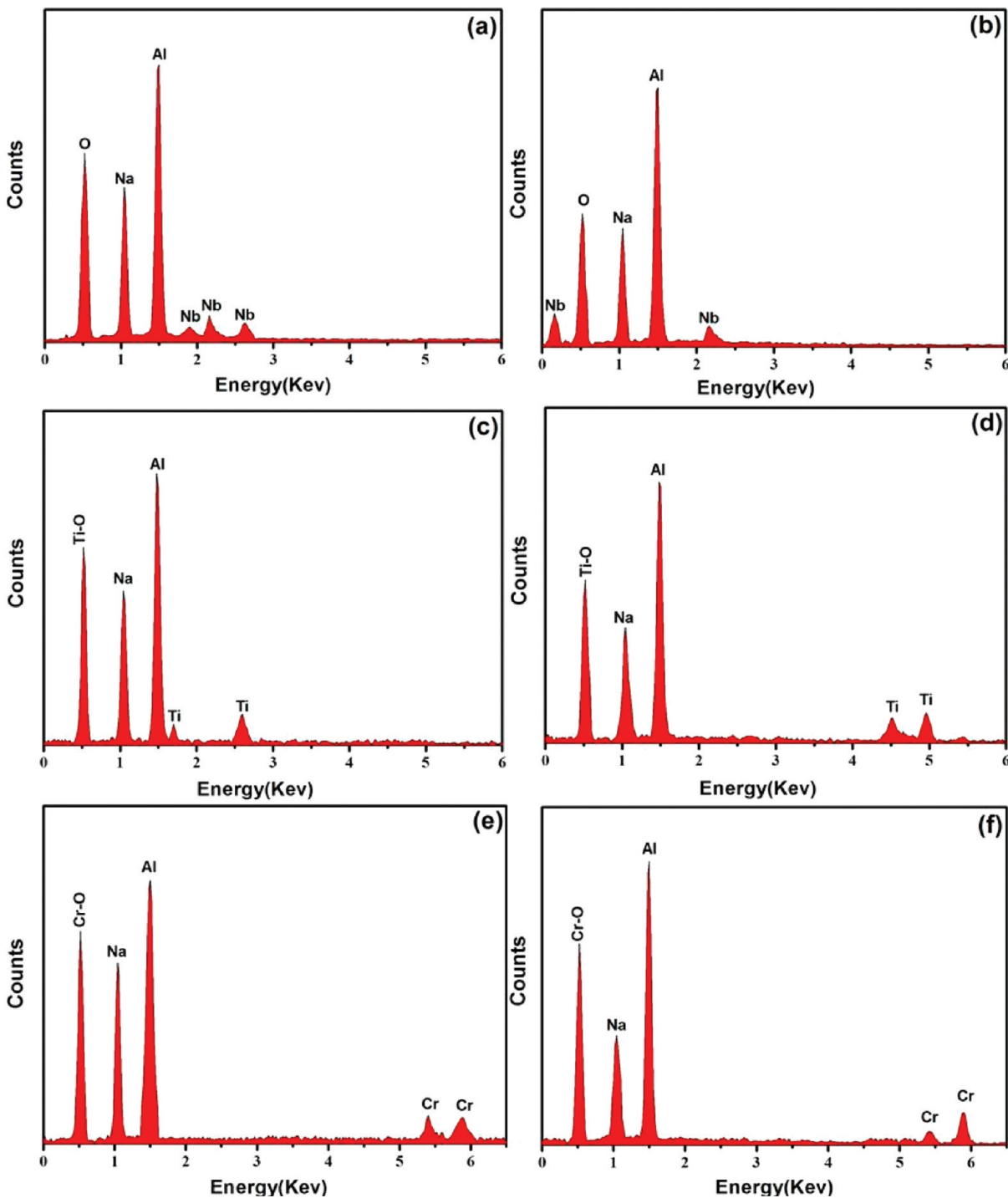


Figure 13. Energy-dispersive spectroscopy (EDS) results of (a) Nb_2O_5 -doped NaAlH_4 after ball milling (area circled in Figure 12a), (b) Nb_2O_5 -doped NaAlH_4 after the third dehydrogenation (area circled in Figure 12b), (c) TiO_2 -doped NaAlH_4 after ball milling (area circled in Figure 12c), (d) TiO_2 -doped NaAlH_4 after the third dehydrogenation (area circled in Figure 12d), (e) Cr_2O_3 -doped NaAlH_4 after ball milling (area circled in Figure 12e), and (f) Cr_2O_3 -doped NaAlH_4 after the third dehydrogenation (area circled in Figure 12f).

surfaces, that is, on oxygen-deficient surfaces. It is believed that the fine dispersion of oxygen-deficient Nb and Ti oxide nanoparticles facilitates the dehydrogenation process by serving as the active sites for nucleation and growth of the dehydrogenated product associated with the shortening of the diffusion paths among the reaction ions. The reabsorption process takes place at the surfaces/interfaces where the niobium and titanium oxide nanoparticles act as a catalyst for dissociation of hydrogen molecules to hydrogen atoms and

transfer them to the surface/interface which act as active nucleation sites for the rehydrogenated products. For Ti-based additives in complex hydride materials like NaAlH_4 (sodium alanate), the formation of active TiAl_3 species on the surface has been proposed as the origin of kinetic improvements in the presence of the additive.⁵⁸ However, no Al-Ti alloy phase can be definitely identified in our XRD as well as XPS examinations of the doped samples. Here the possibility that the Al-Ti alloy

is formed during the milling or cycling process, but presents in an amorphous form, cannot be excluded.

CONCLUSIONS

In conclusion, the nanosized Nb_2O_5 - and TiO_2 -doped Na alanates are shown to have greater and improved hydrogen performance in terms of minimum loss in the cyclic capacity, kinetics, and initial temperature of decomposition, over the undoped as well as nanosized Cr_2O_3 -doped Na alanates. The manometric desorption profiles have revealed that the addition of increasing amounts of Nb_2O_5 and TiO_2 nanoparticles to NaAlH_4 results in a progressive reduction of the onset temperature of NaAlH_4 by as much as 82 and 100 °C for the mixtures containing 5 mol % Nb_2O_5 and TiO_2 , respectively (for pristine NaAlH_4 , it is 178 °C). The apparent activation energy and enthalpy for the first and the second dehydrogenation steps are significantly lowered with Nb_2O_5 and TiO_2 additions, providing quantitative evidence for the decrease in the kinetic and thermodynamic barriers during dehydrogenation. Isothermal desorption results at 150 °C have revealed that enhancements arising upon adding Nb_2O_5 and TiO_2 additions are almost 11–12 times as fast as the undoped NaAlH_4 . In addition, NaAlH_4 with Nb_2O_5 and TiO_2 nanopowders provide cyclic performance better than NaAH_4 with Cr_2O_3 , desorbing about 4.4 wt % hydrogen for 3 h during three cycles. XRD, XPS, FTIR, and FESEM-EDS analyses suggest that hydrogen cycling has induced the reduction of TiO_2 and Nb_2O_5 , which leads to the formation of oxygen-deficient reduced niobium and titanium oxide species. These finely dispersed oxygen-deficient species may contribute to kinetic improvement by facilitating the diffusion of hydrogen through the diffusion barriers in both dehydrogenation and rehydrogenation processes. Moreover, the reduction process of the Ti-based additive during the first desorption is coupled to the migration of the oxygen-deficient reduced titanium oxide species from the surface to the bulk of the material during cycling, where it may limit the grain growth of the formed phases, thus enhancing the kinetics in both discharging and recharging processes by increasing the interfacial area. On the contrary, nano Cr_2O_3 particles act as a surface catalyst and remain stable with much agglomeration during the milling as well as cycling processes.

ASSOCIATED CONTENT

Supporting Information

Figure of XRD profiles of as-received NiAlH_4 and nanosized oxide additives. FESEM images of as-received NaAlH_4 and undoped milled NaAlH_4 . TEM images of as-received metal oxide nanopowders. The results of the first rehydrogenation of the doped samples. Table of various kinetic models examined for the isothermal dehydrogenation curves of Nb_2O_5 - and TiO_2 -doped NaAlH_4 at 120 and 150 °C. This material is available free of charge via the Internet at <http://pubs.acs.org>.

AUTHOR INFORMATION

Corresponding Author

*Tel.: +86-10-62332700. Fax: +86-10-62334311. E-mail: quxh@ustb.edu.cn (Qu Xuanhui); rafi_682@yahoo.com (Rafi-ud-din).

Notes

The authors declare no competing financial interest.

ACKNOWLEDGMENTS

This work is financially supported by the University of Science and Technology Beijing (USTB). The authors also thank the Higher Education Commission (HEC) of Pakistan for the financial support to Rafi-ud-din.

REFERENCES

- (1) Varin, R. A.; Czujko, T.; Wronski, Z. S. *Nanomaterials for Solid State Hydrogen Storage*; Springer Science + Business Media: New York, NY, 2009.
- (2) Yang, J.; Sudik, A.; Wolverton, C.; Siegel, D. *J. Chem. Soc. Rev.* **2010**, *39*, 656.
- (3) Berg, A. W. C.; Arean, C. O. *Chem. Commun.* **2008**, 668.
- (4) Orimo, S.-I.; Nakamori, Y.; Eliseo, J. R.; Züttel, A.; Jensen, C. M. *Chem. Rev.* **2007**, *107*, 4111.
- (5) Rafi-ud-din; Zhang, L.; Ping, L.; Xuanhui, Q. *J. Alloys Compd.* **2010**, *508*, 119.
- (6) Rafi-ud-din; Xuanhui, Q.; Ping, L.; Zhang, L.; Ahmad, M. *J. Phys. Chem. C* **2011**, *115*, 13088–13099.
- (7) Chen, J.; Kuriyama, N.; Xu, Q.; Takeshita, H. T.; Sakai, T. *J. Phys. Chem. B* **2001**, *105*, 11214.
- (8) Fan, X.; Xiao, X.; Chen, L.; Li, S.; Ge, H.; Wang, Q. *J. Phys. Chem. C* **2011**, *115*, 2537.
- (9) Fan, X.; Xiao, X.; Chen, L.; Han, L.; Li, S.; Ge, H.; Wang, Q. *Int. J. Hydrogen Energy* **2011**, *36*, 10861.
- (10) Mao, J. F.; Yu, X. B.; Guo, Z. P.; Poh, C. K.; Liu, H. K.; Wu, Z.; Ni, J. *J. Phys. Chem. C* **2009**, *113*, 10813.
- (11) Zheng, S.; Li, Y.; Fang, F.; Zhou, G.; Yu, X.; Chen, G.; Sun, D.; Ouyang, L.; Zhu, M. *J. Mater. Res.* **2010**, *25*, 2047.
- (12) Xiulin, F.; Xuezhang, X.; Lixin, C.; Shouquan, L.; Qidong, W. *J. Alloys Compd.* **2011**, *509*, 386.
- (13) Sandrock, G.; Gross, K.; Thomas, G. *J. Alloys Compd.* **2002**, *339*, 299.
- (14) Kircher, O.; Fichtner, M. *J. Alloys Compd.* **2005**, *404*, 339.
- (15) Xiao, X.; Chen, L.; Wang, X.; Li, S.; Chen, C.; Wang, Q. *Int. J. Hydrogen Energy* **2008**, *33*, 64.
- (16) Bogdanovic, B.; Schwickardi, M. *J. Alloys Compd.* **1997**, *253–254*, 1.
- (17) Bogdanovic, B.; Brand, R. A.; Marjanovic, A.; Schwickardi, M.; Tolle, J. *J. Alloys Compd.* **2000**, *302*, 36.
- (18) Fichtner, M.; Engel, J.; Fuhr, O.; Kircher, O.; Rubner, O. *Mater. Sci. Eng. B* **2004**, *108*, 42.
- (19) Zheng, S.; Li, Y.; Fang, F.; Zhou, G.; Yu, X.; Chen, G.; Sun, D.; Ouyang, L.; Zhu, M.; Sun, D. *Chem. Mater.* **2008**, *20*, 3954.
- (20) Gao, J.; Adelhelm, P.; Verkuijlen, M. H. W.; Rongeant, C.; Herrich, M.; Bentum, P. J. M. V.; Gutfleisch, O.; Kentgens, A. P. M.; Jong, K. P. D.; Jongh, P. E. D. *J. Phys. Chem. C* **2010**, *114*, 4675.
- (21) Wang, J.; Ebner, A. D.; Ritter, J. A. *J. Phys. Chem. C* **2006**, *110*, 17353.
- (22) Huang, C. K.; Zhao, Y. J.; Sun, T.; Guo, J.; Sun, L. X.; Zhu, M. *J. Phys. Chem. C* **2009**, *113*, 9936.
- (23) Wang, P.; Kang, X. D.; Cheng, H. M. *J. Appl. Phys.* **2005**, *98*, 074905.
- (24) Hudson, M. S. O.; Raghubanshi, H.; Pukazhselvan, D.; Srivastava, O. N. *Int. J. Hydrogen Energy* **2012**, *37*, 2750.
- (25) Adelhelm, P.; Gao, J.; Verkuijlen, M. H. W.; Rongeant, C.; Herrich, M.; Bentum, P. J. M. V.; Gutfleisch, O.; Kentgens, A. P. M.; Jong, K. P. D.; Jongh, P. E. D. *Chem. Mater.* **2010**, *22*, 2233.
- (26) Fan, X. L.; Xiao, X. Z.; Chen, L. X.; Yu, K. R.; Wu, Z.; Li, S. Q.; et al. *Chem. Commun.* **2009**, *44*, 6857.
- (27) Sun, T.; Zhou, B.; Wang, H.; Zhu, M. *Int. J. Hydrogen Energy* **2008**, *33*, 2260.
- (28) Zheng, X. P.; Liu, S. L.; Li, D. L. *Int. J. Hydrogen Energy* **2009**, *34*, 2701.
- (29) Bogdanovic, B.; Felderhoff, M.; Pommerina, A.; Schuth, F.; Spielkamp, N.; Starka, A. *J. Alloys Compd.* **2009**, *471*, 383.
- (30) Schmidt, T.; Rontzsch, L.; Weißgarber, T.; Kieback, B. *Int. J. Hydrogen Energy* **2012**, *37*, 4194.

- (31) Mao, J. F.; Guo, Z. P.; Liu, H. *Int. J. Hydrogen Energy* **2011**, *36*, 14503.
- (32) Leon, A.; Yalovega, G.; Soldatov, A.; Fichtner, M. *J. Phys. Chem. C* **2008**, *112*, 12545.
- (33) Gomes, S.; Renaudin, G.; Hagemann, H.; Yvon, K.; Sulic, M. P.; Jensen, C. M. *J. Alloys Compd.* **2005**, *390*, 305.
- (34) Fang, F.; Zhang, J.; Zhu, J.; Chen, G.; Sun, D.; He, B.; et al. *J. Phys. Chem. C* **2007**, *111*, 3476.
- (35) Xiao, X.; Fan, X.; Yu, K.; Li, S.; Chen, C.; Wang, Q.; Chen, L. *J. Phys. Chem. C* **2009**, *113*, 20745.
- (36) Lee, G.-J.; Shim, J.-H.; Cho, Y. W.; Lee, K. S. *Int. J. Hydrogen Energy* **2007**, *32*, 1911.
- (37) Rongeat, C.; Scheerbaum, N.; Schultz, L.; Gutfleisch, O. *Acta Mater.* **2011**, *59*, 1725.
- (38) Wang, P.; Kang, X. D.; Cheng, H. M. *J. Alloys Compd.* **2006**, *421*, 217.
- (39) Wang, Y. P.; Ren, Q. L.; Wang, Y. J.; Li, L.; Song, D. W.; Jiao, L. F.; et al. *Int. J. Hydrogen Energy* **2010**, *35*, 11004.
- (40) Pukazhselvan, D.; Hudson, M.; Sinha, A.; Srivastava, O. *Energy* **2010**, *35*, 5037.
- (41) Naik, M. D.; Rather, S.; Zacharia, R.; So, C. S.; Hwang, S. W.; Kim, A. R.; Nahm, K. S. *J. Alloys Compd.* **2009**, *471*, L16.
- (42) Seayad, A. M.; Antonelli, D. M. *Adv. Mater.* **2004**, *16*, 765.
- (43) Kang, X. D.; Wang, P.; Cheng, H. M. *J. Appl. Phys.* **2006**, *100*, 034914.
- (44) Bogdanovic, B.; Felderhoff, M.; Kaskel, S.; Pommerin, A.; Schlichte, K.; Schuth, F. *Adv. Mater.* **2003**, *15*, 1012.
- (45) Kim, J. W.; Shim, J.-H.; Kim, S. C.; Remhof, A.; Borgschulte, A.; et al. *J. Power Sources* **2009**, *192*, S82.
- (46) Lee, G.-J.; Shim, J.-H.; Cho, Y. W.; Lee, K. S. *Int. J. Hydrogen Energy* **2008**, *33*, 3748.
- (47) Croston, D. L.; Grant, D. M.; Walker, G. S. *J. Alloys Compd.* **2010**, *492*, 251.
- (48) Patah, A.; Takasaki, A.; Szmyd, J. S. *Int. J. Hydrogen Energy* **2009**, *34*, 3032.
- (49) Friedrichs, O.; Sánchez-López, J. C.; López-Cartes, C.; Klassen, T.; Bormann, R.; Fernández, A. *J. Phys. Chem. B* **2006**, *110*, 7845.
- (50) Mashkoor, A.; Rafi, -ud-Din; Caofeng, P.; Jing, Z. *J. Phys. Chem. C* **2010**, *114*, 2560.
- (51) Kissinger, H. E. *Anal. Chem.* **1958**, *29*, 1702.
- (52) Lee, E.-K.; Cho, Y. W.; Yoon, J. K. *J. Alloys Compd.* **2006**, *416*, 245.
- (53) Lee, B. M.; Jang, J. W.; Shim, J. K.; Cho, Y. W.; Lee., B. J. *J. Alloys Compd.* **2006**, *424*, 36.
- (54) Kamruddin, M.; Ajikumar, P. K.; Dash, S.; Krishnan, R.; Tyagi, A. K.; Krishan, K. *Thermochim. Acta* **1996**, *287*, 13.
- (55) Mahfouz, R. M.; Al-Shehri, S. M.; Monshi, M. A. S.; El-salam, A. B. D. *Radiat. Eff. Defects Solids* **2002**, *157*, 515.
- (56) <http://srdata.nist.gov/xps/>; (accessed Feb 2012).
- (57) Bureau, J. C.; Amri, Z.; Claudy, P.; Letoffe, J. M. *Mater. Res. Bull.* **1989**, *24*, 23.
- (58) Balde, C. P.; Stil, H. A.; van der Eerden, A. M. J.; Jong, K. P.; Bitter, J. H. *J. Phys. Chem. C* **2007**, *111*, 2797.